Supplemental document: Metasurface Optics with on-axis Polarization Control for Terahertz Sensing Application[1]

Supplement Section S1: Algorithm for metasurface pattern generation

The algorithm to generate the metasurface pattern was written in python using the *gdsCAD* documentation, as summarized in Fig. S1 [1]. Initial design parameters had to be chosen: the pattern extent (circular area with R_{MS} of 11 mm); the two grating constants g_1, g_2; and the respective OPP to carry the desired phase functions $\varphi_1(x_l, y_l)$, $\varphi_2(x_l, y_l)$ of (1) in the main text. The simulation results ($W_x(m)$, $\varphi_x(m)$, $T_x(m)$, $W_y(m)$, $\varphi_y(m)$, $T_y(m)$) for each meta-pillar geometry m were imported into the 'meta-pillar library'. Hexagonal lattice points l=(x_l, y_l) with 40 µm spacing were generated within the pattern extent. The algorithm looped over each lattice point l and calculated the phase shifts $\varphi_{aim,x}(l)$, $\varphi_{aim,y}(l)$ to be imposed by the pillar's widths W_x, W_y, as well as the pillar's in-plane rotation angle $\theta_{aim}(l)$ according to (S1**)**, (S2**)** and (S3**)**, respectively.

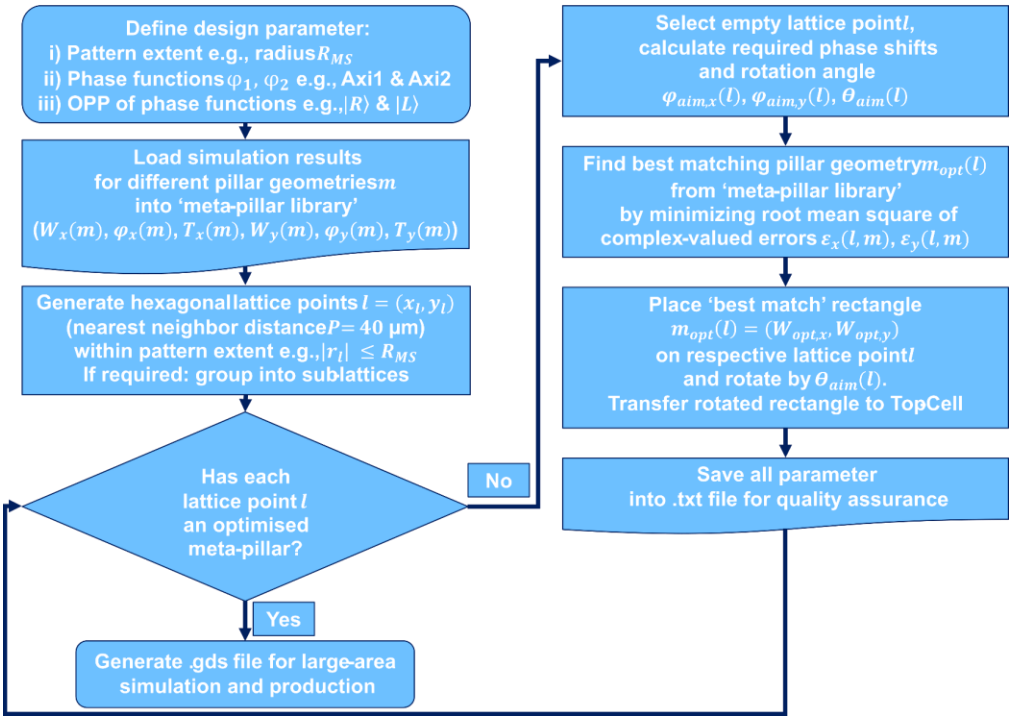

[1] Authors: Thomas S. Nowack (corresponding author: thomas.nowack@glasgow.ac.uk), James P. Grant, Ivonne Escorcia, Mitchell Kenney, Edward Wasige and David R. S. Cumming are with the James Watt School of Engineering, University of Glasgow, United Kingdom. Yash D. Shah and Daniele Faccio are with the School of Physics and Astronomy, University of Glasgow, United Kingdom.

This project has received funding from the European Union's Horizon 2020 research and innovation programme under the Marie Skłodowska-Curie grant agreement No. 765426 (TeraApps) and the UK Quantum Technology Hub in Quantum Imaging (EP/T00097X/1).

DOI of supplement & underlying Data: http://dx.doi.org/10.5525/gla.researchdata.1407
DOI of associated journal article: https://doi.org/10.1109/TTHZ.2023.3263648

Fig. S1. Flowchart for the algorithm to generate metasurface pattern in python using the gdsCAD documentation [1].

$$\boldsymbol{\varphi_{aim,x}(l)} = \begin{cases} \boldsymbol{\varphi_1(l)} & \boldsymbol{for\ OPP\ of\ |D\rangle, |A\rangle} \\ \boldsymbol{0.5 \cdot [\varphi_1(l) + \varphi_2(l)]} & \boldsymbol{for\ OPP\ of\ |R\rangle, |L\rangle} \end{cases} \quad \textbf{(S1)}$$

$$\boldsymbol{\varphi_{aim,y}(l)} = \begin{cases} \boldsymbol{\varphi_2(l)} & \boldsymbol{for\ OPP\ of\ |D\rangle, |A\rangle} \\ \boldsymbol{0.5 \cdot [\varphi_1(l) + \varphi_2(l)] - \pi} & \boldsymbol{for\ OPP\ of\ |R\rangle, |L\rangle} \end{cases} \quad \textbf{(S2)}$$

$$\boldsymbol{\theta_{aim}(l)} = \begin{cases} \boldsymbol{45°\ (const.)} & \boldsymbol{for\ OPP\ of\ |D\rangle, |A\rangle} \\ \boldsymbol{0.25 \cdot [\varphi_1(l) - \varphi_2(l)]} & \boldsymbol{for\ OPP\ of\ |R\rangle, |L\rangle} \end{cases} \quad \textbf{(S3)}$$

The respective equations for independent phase encoding on to an OPP of $|R\rangle$ and $|L\rangle$ were obtained as detailed in the supplement of Devlin et al. [2]. The optimal pillar geometry $m_{opt}(l) = \left(W_{opt,x}(l), W_{opt,y}(l)\right)$ was determined by minimizing the root mean square of the complex-valued errors $\varepsilon_x(l,m)$, $\varepsilon_y(l,m)$, see (S4**)** and (S5**)**, with the imaginary unit j.

$$\boldsymbol{\varepsilon_{x(y)}(l,m)} = \left| \boldsymbol{T_{x(y)}(m) \cdot exp\left[j\, \varphi_{x(y)}(m) \right] - exp\left[j\, \varphi_{aim,x(y)}(l) \right]} \right| \quad \textbf{(S4)}$$

$$\boldsymbol{m_{opt}(l) = Min\left(\sqrt{\left[\varepsilon_x^2(l,m) + \varepsilon_y^2(l,m) \right]/2} \right)} \quad \textbf{(S5)}$$

Supplement Section S2: Monolithic metasurface fabrication

We developed a single-step photolithographic process to dry etch the metasurface layer monolithically into the bulk of silicon substrates (> 10'000 Ωcm, 25 mm x 25 mm, 535 µm thick). The cleaned substrates were dried in an oven before applying the primer (MCC80/20) and resist (SPR220.7) via spin-coating. The resist was soft baked after a relaxation delay and left to rehydrate. Exposure was done through a Cr-mask in hard contact using an i-line mask aligner. After the N_2-loss delay, a post-exposure bake was done before the pattern was developed in CD-26. Residues were ashed in O_2 plasma before the exposed silicon was dry etched (Oxford Instruments, PlasmaPro 100 Estrelas) using an ICP-DRIE Bosch process employing C_4F_8/SF_6 plasma chemistry [3-5]. Optical interference profilometry was employed for measurements of the average etch depth with or without resist on top of the pillars, as described in section 2 B of the main text. This allowed for a second etch to reach completion in case of under-etched samples. The samples were briefly ashed in O_2 plasma once the targeted etch depth of 150 µm was confirmed, after which the resist was stripped in SVC-14.

Supplement Section S3: Performance degradation due to etch depth deviation

The simulations of different pillar geometries $\left(W_x, W_y\right) \in [15\ \mu m; 30\ \mu m]$ shown in Fig. 1 (c) of the main text were repeated for a range of different pillar heights (H $\pm$ ΔH) encountered in practice while accounting for the associated change of the substrate thickness to quantify the impact of the etch depth deviation on the optical performance of fabricated metasurfaces. The deviations of the transmitted x-polarized phase shift $\Delta\varphi_x(\Delta H) = \varphi_x(H) - \varphi_x(H \pm \Delta H)$ caused by height deviations ΔH of $\pm$5 µm and $\pm$10 µm are depicted in Fig. S2 (a)-(d) as function of the pillar dimensions W_x, W_y. One can conclude from the simulation results of Fig. S2:

i) The phase deviation $\Delta\varphi_x(\Delta H)$ changes gradually throughout different pillar dimensions W_x, W_y for all pillar heights H $\pm$ ΔH in Fig. S2 (a)-(d).

ii) The phase deviation of each pillar geometry changes in good approximation linearly with the pillar height $\Delta\varphi_x \propto \Delta H$ from -10 µm to $+10$ µm. Fig. S2 (e) shows the slope for each pillar geometry obtained from a linear fit using the five simulated phase shifts $\varphi_x\left(W_x, W_y, [H \pm \Delta H]\right)$ at different pillar heights (140 µm, 145 µm, 150 µm, 155 µm, 160 µm), whereas Fig. S2 (f) shows the *Pearson correlation coefficient r* for these linear fits. This clear

linear relation between pillar height H and imparted phase shift φ_x is expected from the theory of propagation phase, see (S6) with the pillar's effective refractive index $n_{eff}(W_x, W_y)$, see (2) of Khorasaninejad et al. [6].

$$\boldsymbol{\varphi_{x,y} = \frac{2\pi}{\lambda_0} H \cdot n_{eff}(W_x, W_y)} \qquad \textbf{(S6)}$$

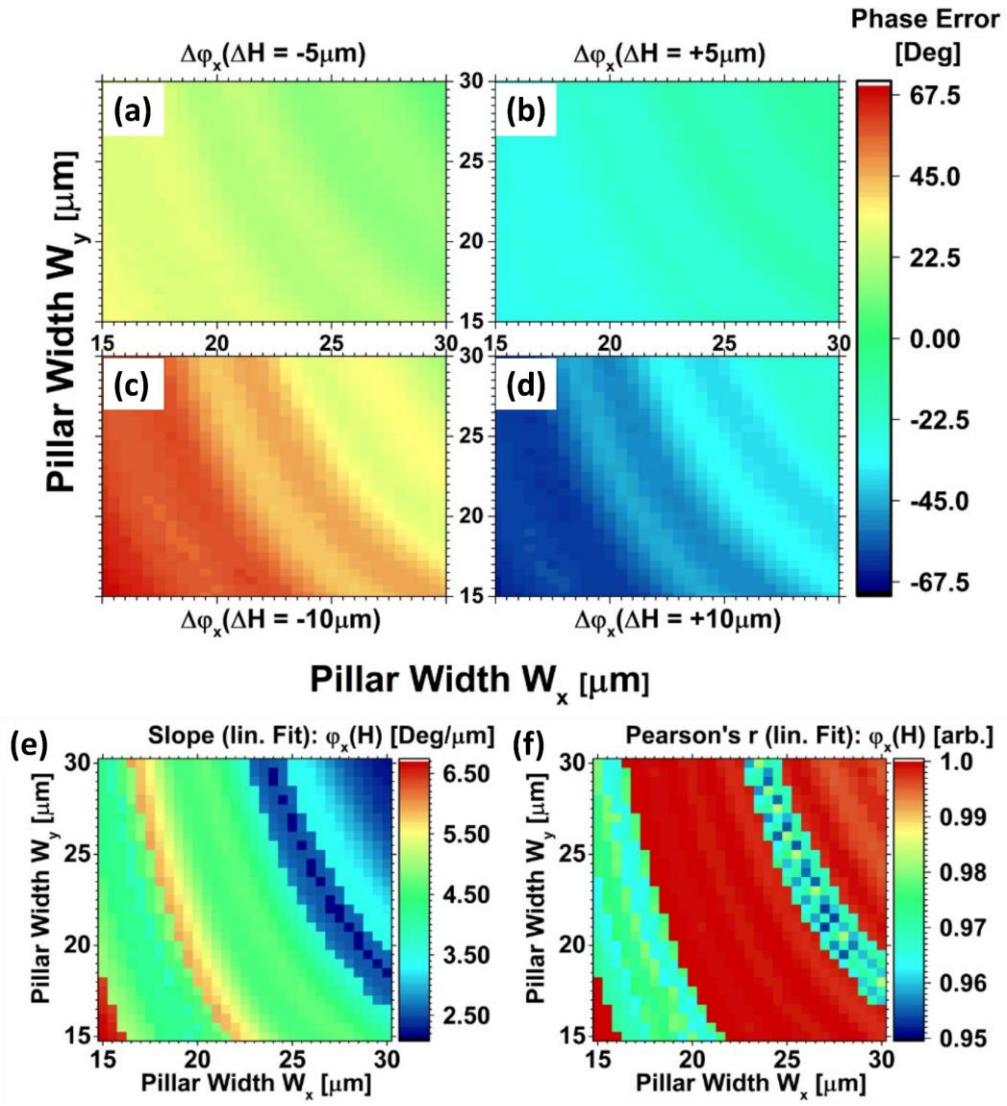

Fig. S2. Simulation results of the phase deviation $\Delta\varphi_x(\Delta H)$ expected for over- and under-etching due to ARDE for height deviations ΔH of (a) $-5\ \mu m$, (b) $+5\ \mu m$, (c) $-10\ \mu m$ and (d) $+10\ \mu m$. For each pillar dimension, the five results of $\varphi_x(H)$ and $\varphi_x(H \pm \Delta H)$ were used for a linear regression whose (e) slope and (f) Pearson correlation coefficient r are shown. Respective results for y-polarized light $\Delta\varphi_y(\Delta H)$ are obtained by swapping the x- and y-axes.

Supplement Section S4: Design of the telecentric 7.7x objective

The commercial software Zemax *OpticStudio* was used to design and optimize the 7.7x telecentric objective, see simulation file. The objective lens was composed of two identical plano-convex TPX lenses (TYDEX) with nominal focal length of 50 mm (40.9 mm simulated

at λ_0) that were optimized to collimate ray bundles originating from the object plane situated 10 mm in front of the first lens's flat surface. The curved surfaces of both lenses were facing each other with 20.5 mm separation. The collimated beam was focused on to the image plane by the tube lens, a plano-convex TPX lens (BATOP) with 250 mm nominal focal length (237.7 mm simulated at λ_0). The tube lens was 210 mm behind the flat surface of the second objective lens and 237 mm before the image plane. n_{TPX} ≈1.46 RIU was taken from [7].

Supplement Section S5: Data acquisition and polarimetric analysis

Our experiments used a sequential measurement procedure for the SoP that required only a single rotating quarter-wave plate (QWP) followed by a fixed polarizer, known as rotating QWP method [8] (see Fig. 4 of the main text). The camera sensor was calibrated and zeroed with blocked beam path before every SoP measurement. Every snapshot image within a SoP measurement was averaged over 60 frames at 50 Hz while the average beam power detected in the reference arm $I_{ref,n}$ was noted. The QWP was rotated in increments of $\Delta\gamma = 180°/N$ before the next snapshot was taken until all $N = 8$ snapshots had been obtained. Every pixel therefore performs an individual SoP measurement generated from the N constituent intensity measurements with successively increased QWP angle of $\gamma_{n+1} = \gamma_n + \Delta\gamma$, ($\gamma_1 = 0°$).

All 8 snapshot images were imported into Matlab with their respective reference beam power $I_{ref,n}$. Every individual snapshot n was zeroed columnwise (col) with the minimum raw pixel value $Min\,[I_{raw,n}(col)]$ of each respective column because the employed bolometric sensor showed a column-dependent increase of its dark count over time. Every pixel of a snapshot n was then scaled by a factor accounting for power fluctuation of the reference beam $I_{ref,n}$ relative to the maximum power detected during the 8 measurements $Max[I_{ref,n}]$, (S7**)**.

$$\boldsymbol{I_n(col) = \left(I_{raw,n}(col) - Min\,[I_{raw,n}(col)]\right) \cdot \frac{Max\,[I_{ref,N}]}{I_{ref,n}}} \qquad \textbf{(S7)}$$

The obtained intensity matrices I_n were used to determine the A, B, C and D matrices according to (S8**)** – (S11**)** [8].

$$\boldsymbol{A = \frac{2}{N}\sum_{n=1}^{N=8} I_n} \qquad \textbf{(S8)}$$

$$\boldsymbol{B = \frac{4}{N}\sum_{n=1}^{N=8} I_n\, sin(2\gamma_n)} \qquad \textbf{(S9)}$$

$$\boldsymbol{C = \frac{4}{N}\sum_{n=1}^{N=8} I_n\, cos(4\gamma_n)} \qquad \textbf{(S10)}$$

$$\boldsymbol{D = \frac{4}{N}\sum_{n=1}^{N=8} I_n\, sin(4\gamma_n)} \qquad \textbf{(S11)}$$

Care had to be taken to calculate the partially polarized Stokes parameter S_0^* to S_3^* since our fixed polarizer transmitted |V⟩ polarized light as opposed to the |H⟩ described in [8]. To correct for the polarizer's 90º "misalignment", an additional $sgn(-)$ in had to be inserted in (S13**)**, (S14**)** and (S15**)**, as described by (7) of Flueraru et al. [9].

$$\boldsymbol{S_0^* = A - C} \qquad \textbf{(S12)}$$

$$\boldsymbol{S_1^* = -(2C)} \qquad \textbf{(S13)}$$

$$\boldsymbol{S_2^* = -(2D)} \qquad \textbf{(S14)}$$

$$\boldsymbol{S_3^* = -(B)} \qquad \textbf{(S15)}$$

After calculating the degree of polarization (DOP) in (S16**)**, the fully polarized Stokes Parameter S_0 to S_3 (normalized by S_0) can be calculated in (S17**)** to (S20**)**. In turn, the characteristic angles of the polarization ellipse can be calculated with (S21**)** and (S22**)**, namely the orientation angle ψ and ellipticity angle χ, respectively. The resulting image matrices of (S16**)** to (S22**)** were consequently smoothened with a 3-by-3 median filter using the Matlab function "*medfilt2(Data,[3 3])"*.

$$\boldsymbol{DOP = \frac{\sqrt{S_1^{*2} + S_2^{*2} + S_3^{*2}}}{S_0^*}} \quad \textbf{(S16)}$$

$$\boldsymbol{S_0 = \frac{S_0^*}{DOP} - \frac{(1 - DOP)}{DOP}} \quad \textbf{(S17)}$$

$$\boldsymbol{S_1 = \frac{S_1^*}{DOP \cdot S_0}} \quad \textbf{(S18)}$$

$$\boldsymbol{S_2 = \frac{S_2^*}{DOP \cdot S_0}} \quad \textbf{(S19)}$$

$$\boldsymbol{S_3 = \frac{S_3^*}{DOP \cdot S_0}} \quad \textbf{(S20)}$$

$$\boldsymbol{\Psi = \frac{1}{2} tan^{-1}\left(\frac{S_2}{S_1}\right) \quad (0 < \Psi \leq \pi)} \quad \textbf{(S21)}$$

$$\boldsymbol{\chi = \frac{1}{2} tan^{-1}\left(\frac{S_3}{\sqrt{S_1^{\,2} + S_2^{\,2}}}\right) \quad \left(-\frac{\pi}{4} < \chi \leq \frac{\pi}{4}\right)} \quad \textbf{(S22)}$$

References

[1] A. G. Mark. "gdsCAD's documentation." https://pythonhosted.org/gdsCAD/ (accessed 11 September, 2022).

[2] R. C. Devlin *et al.*, "Spin-to-orbital angular momentum conversion in dielectric metasurfaces," *Opt Express,* vol. 25, no. 1, pp. 377-393, Jan 9 2017, doi: 10.1364/OE.25.000377.

[3] B. Chang, P. Leussink, F. Jensen, J. Hübner, and H. Jansen, "DREM: Infinite etch selectivity and optimized scallop size distribution with conventional photoresists in an adapted multiplexed Bosch DRIE process," *Microelectronic Engineering,* vol. 191, pp. 77-83, 2018, doi: 10.1016/j.mee.2018.01.034.

[4] H. V. Jansen, M. J. de Boer, S. Unnikrishnan, M. C. Louwerse, and M. C. Elwenspoek, "Black silicon method: X. A review on high speed and selective plasma etching of silicon with profile control: an in-depth comparison between Bosch and cryostat DRIE processes as a roadmap to next generation equipment," *Journal of Micromechanics and Microengineering,* vol. 19, no. 3, 2009, doi: 10.1088/0960-1317/19/3/033001.

[5] F. Stöhr *et al.*, "Sacrificial structures for deep reactive ion etching of high-aspect ratio kinoform silicon x-ray lenses," *Journal of Vacuum Science & Technology B, Nanotechnology and Microelectronics: Materials, Processing, Measurement, and Phenomena,* vol. 33, no. 6, 2015, doi: 10.1116/1.4931622.

[6] M. Khorasaninejad *et al.*, "Polarization-Insensitive Metalenses at Visible Wavelengths," *Nano Lett,* vol. 16, no. 11, pp. 7229-7234, Nov 9 2016, doi: 10.1021/acs.nanolett.6b03626.

[7] V. E. Rogalin, I. A. Kaplunov, and G. I. Kropotov, "Optical Materials for the THz Range," *Optics and Spectroscopy,* vol. 125, no. 6, pp. 1053-1064, 2019, doi: 10.1134/s0030400x18120172.

[8] B. Schaefer, E. Collett, R. Smyth, D. Barrett, and B. Fraher, "Measuring the Stokes polarization parameters," (in English), *American Journal of Physics,* vol. 75, no. 2, pp. 163-168, Feb 2007, doi: 10.1119/1.2386162.

[9] C. Flueraru, S. Latoui, J. Besse, and P. Legendre, "Error Analysis of a Rotating Quarter-Wave Plate Stokes' Polarimeter," *IEEE Transactions on Instrumentation and Measurement,* vol. 57, no. 4, pp. 731-735, 2008, doi: 10.1109/tim.2007.913752.